REPORT

MAGNETISM

Probing magnetism in 2D materials at the nanoscale with single-spin microscopy

L. Thiel[1], Z. Wang[2,3], M. A. Tschudin[1], D. Rohner[1], I. Gutiérrez-Lezama[2,3], N. Ubrig[2,3], M. Gibertini[2,4], E. Giannini[2], A. F. Morpurgo[2,3], P. Maletinsky[1]*

The discovery of ferromagnetism in two-dimensional (2D) van der Waals (vdW) crystals has generated widespread interest. Making further progress in this area requires quantitative knowledge of the magnetic properties of vdW magnets at the nanoscale. We used scanning single-spin magnetometry based on diamond nitrogen-vacancy centers to image the magnetization, localized defects, and magnetic domains of atomically thin crystals of the vdW magnet chromium(III) iodide (CrI_3). We determined the magnetization of CrI_3 monolayers to be ≈16 Bohr magnetons per square nanometer, with comparable values in samples with odd numbers of layers; however, the magnetization vanishes when the number of layers is even. We also found that structural modifications can induce switching between ferromagnetic and antiferromagnetic interlayer ordering. These results demonstrate the benefit of using single-spin scanning magnetometry to study the magnetism of 2D vdW magnets.

Magnetism in individual monolayers of van der Waals (vdW) crystals has recently been observed in a range of materials, including semiconducting (*1*, *2*) and metallic (*3*–*5*) compounds. The discovery of such two-dimensional (2D) magnetic order is nontrivial (*6*) and has garnered considerable attention owing to emerging exotic phenomena such as magnetoelectric effects (*7*–*10*) or potential, 2D Kitaev spin liquids (*11*, *12*). Two-dimensional magnets have been used as functional elements in spintronics; examples include spin filters (*13*, *14*), spin transistors (*15*), tunneling magnetoresistance devices (*16*, *17*), and magnetoelectric switches (*8*–*10*). Quantitative study of the magnetic response of these atomically thin crystals at the nanoscale is highly desirable, but the required experimental methods are still lacking. Indeed, transport experiments (*8*, *9*, *13*–*16*) probe magnetic properties only indirectly. Spatially resolved studies rely on optical techniques, such as fluorescence (*18*, *19*) or the magneto-optical Kerr effect (MOKE) (*1*, *2*, *4*), and are therefore limited to the micrometer scale. Even more critically, these techniques do not provide quantitative information about magnetization [MOKE, for instance, may yield nonzero signals even for antiferromagnets (*20*)] and are susceptible to interference effects that may obscure magnetic signals in thin samples (*1*).

We overcame these limitations and employed a scanning nitrogen-vacancy (NV) center spin in diamond as a sensitive, atomic-scale magnetometer (*21*) to quantitatively determine key magnetic properties of CrI_3 and to directly image magnetic domains with spatial resolutions of a few tens of nanometers. For magnetometry, we exploited the Zeeman effect, which led to a shift of the NV spin's energy levels as a function of magnetic field. In the regime relevant for this work, the NV spin shows a linear Zeeman response for magnetic fields B_{NV} along its spin-quantization axis $\vec{e}_{NV}$ (Fig. 1A), whereas it is largely insensitive to fields orthogonal to $\vec{e}_{NV}$ (*21*). The NV spin therefore offers a direct and quantitative measurement of the vectorial component B_{NV} of stray magnetic fields emerging from a sample.

The Zeeman shifts of the involved NV spin-levels can be conveniently read out by optically detected magnetic resonance (ODMR) with 532-nm laser excitation, microwave spin driving, and NV fluorescence detection for spin readout (*22*, *23*). For nanoscale imaging, we employed a single NV spin held in the tip of an atomic force microscope and placed the NV down to a distance z_{NV} ~ 60 nm from the sample, which resulted in a magnetic imaging resolution on the order of z_{NV} (*21*). The scanning probe containing the NV (*24*, *25*) was integrated into a confocal optical microscope for optical spin readout and the whole apparatus immersed in a liquid ^{4}He cryostat. Superconducting magnets were used to enable vectorial magnetic field control up to 0.5 T. The measurement temperature of ~7 K was determined by a resistive thermometer placed near the sample.

We studied CrI_3 samples of various thicknesses, which were encapsulated in either hexagonal

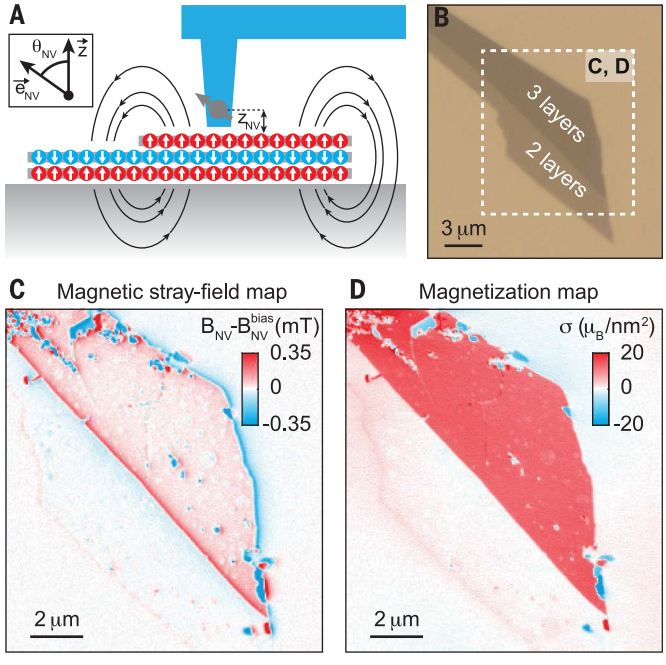

Fig. 1. Nanoscale imaging of magnetism in two-dimensional van der Waals magnets. (**A**) Schematic of the scanning single-spin magnetometry technique employed in this work. A single NV electronic spin is scanned across few-layer flakes of encapsulated CrI_3 (encapsulation not shown). Stray magnetic fields from the sample are sensed by optically detected Zeeman shifts of the NV spin states and imaged with nanoscale resolution (set by the sensor–sample separation z_{NV}) by lateral scanning of the NV. The method detects magnetic fields along the NV spin quantization axis $\vec{e}_{NV}$ at an angle θ_{NV}~54° from the sample normal. (**B**) Optical micrograph of the CrI_3 bi- and trilayer flake of sample D1. (**C**) Magnetic field map of B_{NV} across sample D1 recorded in a bias field $B_{NV}^{bias} = 172.5$ mT and at a typical green laser power $P_{laser} \approx 40$ μW. Strong (or weak) stray fields emerge from the edges of the trilayer (or bilayer) flake. (**D**) Map of magnetization distribution in sample D1, determined by reverse propagation of the magnetic field map in (C) [see text and (*23*)].

[1]Department of Physics, University of Basel, Klingelbergstrasse 82, Basel CH-4056, Switzerland. [2]Department of Quantum Matter Physics, University of Geneva, 24 Quai Ernest Ansermet, CH-1211 Geneva, Switzerland. [3]Group of Applied Physics, University of Geneva, 24 Quai Ernest Ansermet, CH-1211 Geneva, Switzerland. [4]National Centre for Computational Design and Discovery of Novel Materials (MARVEL), École Polytechnique Fédérale de Lausanne, CH-1015 Lausanne, Switzerland.
*Corresponding author. Email: patrick.maletinsky@unibas.ch

boron nitride or graphene to assure the stability of CrI_3 under oxygen atmosphere [for details, see (*23*)]. The samples (Fig. 1B) were fabricated by mechanical exfoliation of CrI_3 and subsequently encapsulated using an established pick-and-place technique (*16*). Samples of various CrI_3 thicknesses in the range of a few (<10) layers were produced to study the effect of thickness on magnetic ordering. For each CrI_3 sample, the number of atomic layers was determined by a combination of atomic force microscopy and optical microscopy (*23*). For preparation and analysis of the magnetic state of CrI_3, the samples were mounted in the NV magnetometer and cooled in zero magnetic field to the final measurement temperature.

Figure 1C shows a typical magnetic field map acquired on an area containing bilayer and trilayer CrI_3 (sample D1). The presented data were acquired in a bias field $B_{NV}^{bias} = 172.5$ mT, where magnetometer performance was optimal, but similar images and results were found at lower fields as well (fig. S7). We obtained such maps from NV ODMR spectra acquired at each pixel (acquisition time ≈2 s per pixel), from which we determined B_{NV} through a fit (*23*). We confirmed experimentally that for typical parameters used in our study, our approach induced no appreciable back-action onto the sample (e.g., through heating by laser illumination or microwave irradiation) (*23*). The resulting data show stray magnetic fields emerging predominantly from the edges of the trilayer flake, as expected for a largely uniform magnetization (*26*), and thereby provide evidence for the magnetization of few-layer CrI_3.

To reveal further details of the underlying magnetization pattern in CrI_3, we used well-established reverse-propagation protocols (*27*) to map the magnetic field image of B_{NV} to its source [see (*23*) for details]. For a 2D, out-of-plane magnetization, as in the present case, such reverse propagation yields a unique determination of the underlying magnetization pattern (Fig. 1D), provided that the distance z_{NV} between sensor and sample is known. In our refined reverse-propagation protocol, we determine z_{NV} through an iterative procedure described in the supplementary materials and a recent study by Appel *et al.* (*23*, *28*). The reverse propagation thereby additionally yields the spatial resolution of our magnetic field and magnetization images, which is directly given by z_{NV} (for the data in Fig. 1, z_{NV} = 62 nm). In the following paragraphs, we focus our discussion on magnetization maps obtained through such reverse propagation; the raw magnetic field images are presented in the supplementary materials (*23*).

The magnetization pattern in Fig. 1D clearly shows a largely homogeneous magnetization for this trilayer CrI_3 flake, which is typical for most samples that we investigated. In addition, sparsely scattered, localized defects, mostly with vanishing magnetization, were visible across the flake, and several irregularities occurred at the flake edges, which were likely caused by curling and rippling induced on the edges during sample preparation. On the flake, we found an average magnetization $\sigma_z \approx (13.0 \pm 2.4)\mu_B/nm^2$ (with μ_B the Bohr magneton), consistent with a single layer of fully polarized Cr^{+3} spins, for which $\sigma_z^{mono} = 14.7\mu_B/nm^2$ would be expected (*29*). The data thus support the notion of antiferromagnetic interlayer exchange coupling in few-layer CrI_3 (*1*), which results in a net magnetization σ_z^{mono} for a magnetically ordered trilayer sample.

Sample D1 additionally contained a region of bilayer CrI_3 for which we observed zero bulk moment, again consistent with antiferromagnetic interlayer coupling. However, the bilayer also showed weak magnetization located within less than our spatial resolution from the edge (Fig. 1D). The origin of this magnetization is currently unknown but may be related to magnetoelectric effects (*7*, *9*), a narrow region of monolayer CrI_3 protruding from the bilayer, or spin canting (*30*) near the edge of the flake.

We applied our measurement procedure to a variety of samples, including a monolayer and the five- and nine-layer flakes shown in Fig. 2, A, B, and C, respectively. Notably, all of these flakes exhibit near-uniform magnetization at a magnitude comparable to σ_z^{mono}. We additionally determined σ_z in an independent manner by measuring B_{NV} along lines crossing the edges of each flake (Fig. 2, lower panels). Assuming a purely out-of-plane magnetization, analytical fits (*23*) to these data allow for the quantitative determination of both σ_z and z_{NV}. Potential tilting of the magnetization away from z in the vicinity of the edge caused by, for instance, the Dzyaloshinskii-Moriya interaction would lead to negligible deviations from our findings (*31*). For the monolayer, five-, and nine-layer flakes, we find $\sigma_z = (16.1 \pm 0.6)\mu_B/nm^2$, $(16.4 \pm 0.2)\mu_B/nm^2$, and $(14.1 \pm 0.2)\mu_B/nm^2$, respectively, where uncertainties denote statistical errors of the fit [$z_{NV} \approx 60$ nm in all cases, see (*23*)]. The general agreement of these fits with the values of σ_z found in Fig. 2, A to C, further confirms the validity of our reverse-propagation method.

Our observations thus far corroborate previous results of studies of few-layer CrI_3 (*10*, *13*, *19*), which all found CrI_3 flakes with odd (or even) numbers of layers to exhibit nonzero (or near-zero) magnetization as a result of antiferromagnetic interlayer exchange coupling. These observations, however, are in conflict with the established fact that CrI_3 is a bulk ferromagnet (*32*). We shed light on this dichotomy in a subsequent experiment on sample D2, where our diamond scanning probe induced an unintentional local puncture through the encapsulation layer of the CrI_3 flake (Fig. 3A) (*23*). After this incident, the entire sample, up to several micrometers away from the puncture, exhibited a substantially enhanced magnetization, as evidenced by a representative magnetization map (Fig. 3B) and B_{NV} linescan (Fig. 3C) across the flake. The data show a ≈9.7-fold increase of magnetization from initially $(14.1 \pm 0.2)\mu_B/nm^2$ to $(136.9 \pm 0.4)\mu_B/nm^2$. For the nine-layer flake, this enhancement suggests that the puncture induced a transition from antiferromagnetic to ferromagnetic interlayer coupling.

To investigate the possibility of a structural transition in our punctured sample, we compared its low-temperature Raman spectrum with that of a pristine flake, in a spectral region where characteristic Raman modes for CrI_3 exist (Fig. 3D) (*33*). Although the data do not allow for an unambiguous determination of the crystalline structure of our samples, the markedly different spectra clearly point to a change in structure occurring simultaneously with the change in magnetic order discussed above. This observation is consistent with recent results of density

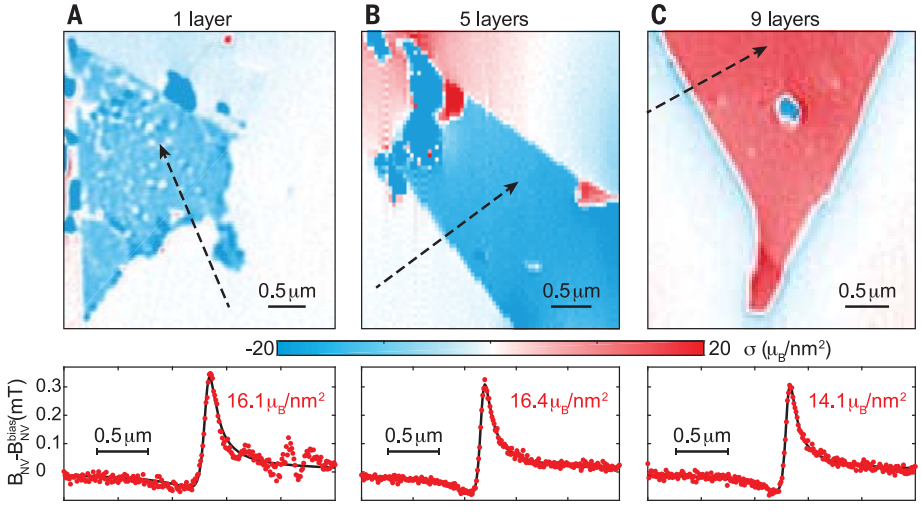

Fig. 2. Magnetization maps of few-layer CrI_3 flakes. Data were acquired after zero-field cooling and spontaneous magnetic ordering under the experimental conditions described in the Fig. 1 legend. Magnetization maps were obtained for (**A**) a monolayer, (**B**) a five-layer-thick sample, and (**C**) a nine-layer-thick sample [see text and (*23*)]. The colorbar applies to all panels. (Bottom) Independently acquired data of magnetic field B_{NV} measured across the borders of each flake, along the lines indicated in the maps. These data allow for an independent determination of magnetization σ_z and sensor–sample separation z_{NV} using analytic fits (black) (*23*).

functional calculations (*16*, *34*–*37*), predicting an interplay between stacking order and interlayer exchange coupling in CrI_3. Further study is needed to elucidate the nature of the structural transition induced by the puncture and the crystalline structure before the puncture.

The connection between crystal structure and magnetism also offers an explanation for the occurrence of magnetic domains in some of our CrI_3 samples. Figure 4A shows a representative image of such domains on sample D2 (nine-layer flake). Notably, the measured domain magnetizations only assume values close to integer multiples of σ_z^{mono}; i.e., $\sigma_z = n\sigma_z^{mono}$, with $n \in \mathbb{Z}$. This observation can be explained by spatial variations (either in-plane or out-of-plane) in the interlayer exchange coupling due to, for instance, local changes in stacking order. Such variations would result in regions with varying numbers of (anti) ferromagnetically coupled CrI_3 layers, consistent with the observed domains. This domain formation mechanism would preserve the parity of n, and we observe well-separated regions on the sample where n is either even or odd (see outlines in Fig. 4A and histogram in Fig. 4B). The removal or addition of a monolayer of CrI_3 between these areas can explain this observation and could have occurred during material exfoliation or sample preparation.

In this study, we used scanning NV magnetometry to observe a direct connection between structural and nanoscale magnetic ordering in CrI_3 and thereby address the question of why few-layer CrI_3 shows antiferromagnetic interlayer exchange coupling despite the bulk being ferromagnetic. Our work establishes scanning NV magnetometry as a powerful tool for addressing nanoscale magnetism in vdW crystals, down to the limit of a single atomic layer. Such direct, quantitative imaging and sensing is vital to advance our understanding of these materials and their development toward applications in future spintronics devices (*3*, *5*). Our approach is general and may even be applied under ambient conditions (*3*, *21*) or to materials that have thus far not been suitable for the application of optical methods (*38*). Finally, the ability to perform NV magnetometry on vdW magnets offers perspectives for high-frequency sensing (*39*) of their magnonic excitations (*14*, *38*), which may enable vdW-based atomic-scale platforms in magnonics applications.

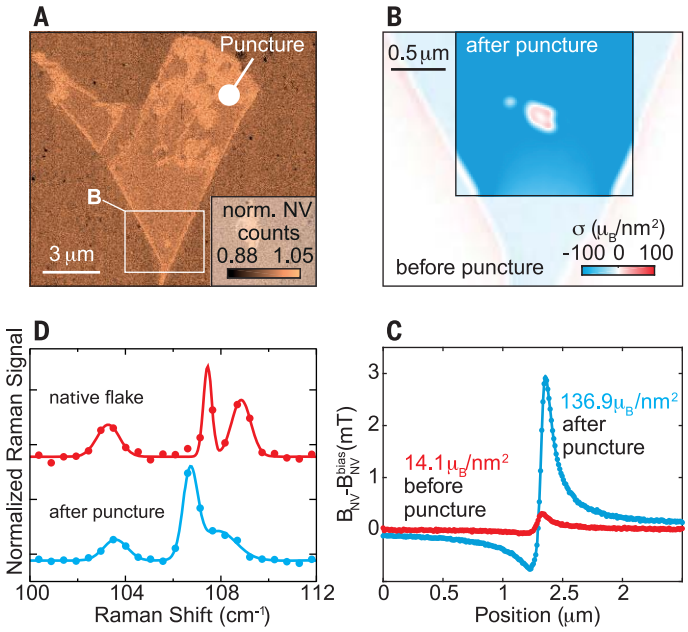

Fig. 3. Interplay of structural and magnetic order in few-layer CrI_3. (**A**) Overview image of sample D2 (*23*), indicating the location of the puncture and the representative region sampled subsequently. The data show normalized NV counts acquired while a fixed-frequency microwave tone was applied (*23*). (**B**) Enhanced magnetization observed in the nine-layer flake of sample D2 after puncture of the CrI_3 encapsulation. The puncture is located a few micrometers from the imaged region [see (A)]. The faint background shows the (inverted) data from Fig. 2C for comparison. The colorbar applies to all data. (**C**) Linecut of B_{NV} across a representative edge of the punctured flake (blue), indicating a magnetization $\sigma_z \approx (136.9 \pm 0.4)\mu_B/nm^2$, which is close to the expected value for a fully polarized nine-layer sample. For reference, the red trace shows the corresponding data from before the puncture. (**D**) Raman spectra from the punctured flake and an unpunctured reference, suggesting the concurrence of a structural transition with the magnetic transition.

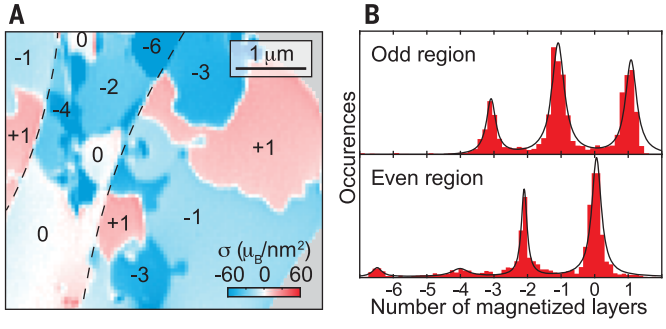

Fig. 4. Magnetic domains in CrI_3. (**A**) Spontaneously occurring magnetic domains observed in the nine-layer flake of sample D2. The magnetization σ_z was found to be discretized in integer multiples of the monolayer magnetization σ_z^{mono}. Numbers indicate σ_z in multiples of σ_z^{mono}, where positive (or negative) values denote magnetizations along the +*z* (or −*z*) direction. A clear separation of the flake into regions of even and odd multiples of σ_z^{mono} is observed. Even-numbered regions are assigned to a missing or added monolayer (see text). Areas where no flake was present were false-colored in gray. Dashed lines indicate the boundary between regions of even and odd multiples of σ_z^{mono}. (**B**) Histograms of magnetization pixel values obtained in the odd- and even-numbered regions of the data in (A).

REFERENCES AND NOTES

1. B. Huang *et al.*, *Nature* **546**, 270–273 (2017).
2. C. Gong *et al.*, *Nature* **546**, 265–269 (2017).
3. M. Bonilla *et al.*, *Nat. Nanotechnol.* **13**, 289–293 (2018).
4. Z. Fei *et al.*, *Nat. Mater.* **17**, 778–782 (2018).
5. Y. Deng *et al.*, *Nature* **563**, 94–99 (2018).
6. N. D. Mermin, H. Wagner, *Phys. Rev. Lett.* **17**, 1133–1136 (1966).
7. Z. Wang *et al.*, *Nat. Nanotechnol.* **13**, 554–559 (2018).
8. S. Jiang, J. Shan, K. F. Mak, *Nat. Mater.* **17**, 406–410 (2018).
9. S. Jiang, L. Li, Z. Wang, K. F. Mak, J. Shan, *Nat. Nanotechnol.* **13**, 549–553 (2018).
10. B. Huang *et al.*, *Nat. Nanotechnol.* **13**, 544–548 (2018).
11. A. Banerjee *et al.*, *Nat. Mater.* **15**, 733–740 (2016).
12. A. Banerjee *et al.*, *Science* **356**, 1055–1059 (2017).
13. T. Song *et al.*, *Science* **360**, 1214–1218 (2018).
14. D. R. Klein *et al.*, *Science* **360**, 1218–1222 (2018).
15. S. Jiang, L. Li, Z. Wang, J. Shan, K. F. Mak, arXiv:1807.04898 [cond-mat.mes-hall] (13 July 2018).
16. Z. Wang *et al.*, *Nat. Commun.* **9**, 2516 (2018).
17. H. H. Kim *et al.*, *Nano Lett.* **18**, 4885–4890 (2018).
18. D. Zhong *et al.*, *Sci. Adv.* **3**, e1603113 (2017).
19. K. L. Seyler *et al.*, *Nat. Phys.* **14**, 277–281 (2018).
20. N. Sivadas, S. Okamoto, D. Xiao, *Phys. Rev. Lett.* **117**, 267203 (2016).
21. L. Rondin *et al.*, *Rep. Prog. Phys.* **77**, 056503 (2014).
22. A. Gruber *et al.*, *Science* **276**, 2012–2014 (1997).
23. See supplementary materials for additional information.
24. P. Maletinsky *et al.*, *Nat. Nanotechnol.* **7**, 320–324 (2012).
25. P. Appel *et al.*, *Rev. Sci. Instrum.* **87**, 063703 (2016).
26. T. Hingant *et al.*, *Phys. Rev. Appl.* **4**, 014003 (2015).
27. B. J. Roth, N. G. Sepulveda, J. P. Wikswo Jr., *J. Appl. Phys.* **65**, 361–372 (1989).
28. P. Appel *et al.*, *Nano Lett.* **19**, 1682–1687 (2019).
29. M. A. McGuire, H. Dixit, V. R. Cooper, B. C. Sales, *Chem. Mater.* **27**, 612–620 (2015).

30. F. Garcia-Sanchez, P. Borys, A. Vansteenkiste, J.-V. Kim, R. L. Stamps, *Phys. Rev. B* **89**, 224408 (2014).
31. J. P. Tetienne *et al*., *Nat. Commun.* **6**, 6733 (2015).
32. J. F. Dillon Jr., C. E. Olson, *J. Appl. Phys.* **36**, 1259–1260 (1965).
33. S. Djurdjić-Mijin *et al*., *Phys. Rev. B* **98**, 104307 (2018).
34. P. Jiang *et al*., *Phys. Rev. B* **99**, 144401 (2019).
35. D. Soriano, C. Cardoso, J. Fernández-Rossier, arXiv:1807.00357 [cond-mat.mes-hall] (1 July 2018).
36. N. Sivadas, S. Okamoto, X. Xu, C. J. Fennie, D. Xiao, *Nano Lett.* **18**, 7658–7664 (2018).
37. S. W. Jang, M. Y. Jeong, H. Yoon, S. Ryee, M. J. Han, *Phys. Rev. Mater.* **3**, 031001(R) (2019).
38. D. Ghazaryan *et al*., *Nat. Electron.* **1**, 344–349 (2018).
39. C. Du *et al*., *Science* **357**, 195–198 (2017).
40. L. Thiel *et al*., Replication Data for: Probing magnetism in 2D materials at the nanoscale with single spin microscopy, Version 1.0, Zenodo (2019); https://dx.doi.org/10.5281/zenodo.2574907.

ACKNOWLEDGMENTS

We thank A. Högele, V. Jacques, M. Munsch, and J.-V. Kim for discussions and feedback on the manuscript and A. Ferreira for technical help. **Funding:** We acknowledge financial support from the SNI; NCCR QSIT; SNF grants 155845, 169016, and 178891; the EU Graphene Flagship project; and the EU Quantum Flagship project ASTERIQS (820394). N.U. and M.G. acknowledge support through an Ambizione fellowship of the SNF (Swiss National Science Foundation). **Author contributions:** All authors contributed to all aspects of this work. **Competing interests:** The authors declare no competing interests. **Data and materials availability:** All data shown in this paper are available at Zenodo (*40*).

SUPPLEMENTARY MATERIALS

science.sciencemag.org/content/364/6444/973/suppl/DC1
Materials and Methods
Supplementary Text
Figs. S1 to S9
Reference (*41*)

10 October 2018; accepted 8 April 2019
Published online 25 April 2019
10.1126/science.aav6926